

Extreme-Parameter Non-Hermitian Dielectric Metamaterials

Marino Coppolaro, Massimo Moccia, Vincenzo Caligiuri, Giuseppe Castaldi, Nader Engheta, and Vincenzo Galdi*

Cite This: <https://dx.doi.org/10.1021/acsphotonics.0c00924>

Read Online

ACCESS |



Metrics & More



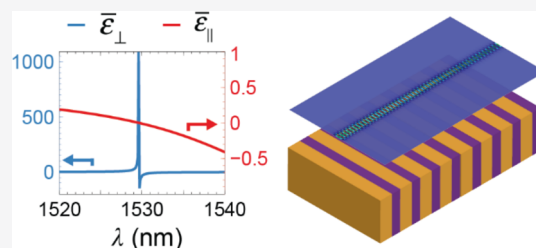
Article Recommendations



Supporting Information

ABSTRACT: The emerging fields of non-Hermitian optics and photonics are inspiring radically new, unconventional ways of mixing active and passive constituents to attain exotic light–matter interactions. Here, inspired by the concept of *parity-time symmetry*, we propose and explore a class of non-Hermitian multilayered metamaterials, featuring spatial modulation of gain and loss, which can exhibit *extreme anisotropy* in the epsilon-near-zero regime. Specifically, via analytic and numerical studies, we investigate the intriguing parameter tunability and wave-propagation effects that can occur in these media due to the delicate interplay between gain and loss. These include, for instance, field canalization, subdiffractive imaging, and reconfigurable waveguiding/radiation, and remarkably, they do not rely on the presence of metallic constituents. Moreover, we show that the extreme-parameter regime of interest is technologically feasible, e.g., in terms of material constituents based on dye-doped indium tin oxide at near-infrared wavelengths. Our outcomes bring about new, largely unexplored dimensionalities and possibilities in the tailoring of the effective properties of non-Hermitian metamaterials and open the door to a wealth of possible developments and applications in reconfigurable nanophotonics scenarios.

KEYWORDS: Non-Hermitian, metamaterials, epsilon near zero, homogenization, nonlocal effects



Metamaterials are artificially structured materials made of subwavelength dielectric and/or dielectric inclusions that can be engineered so as to transcend the basic limitations of their material constituents and exhibit unusual constitutive properties and anomalous light–matter interactions.^{1,2} Prominent among the exotic responses that can be attained is the possibility to exhibit *extreme* (e.g., very small or very large) constitutive parameters.³ For instance, epsilon-near-zero (ENZ) and near-zero-index^{4–12} materials have been proposed and applied to a variety of scenarios, from anomalous tunneling to nonlinear and quantum optics.

Of great interest is the *extreme anisotropy* of the constitutive dielectric tensors, occurring, e.g., in nanowire-based¹³ and metallo-dielectric multilayered^{14–19} metamaterials, which finds important applications especially in subdiffractive imaging. Although in certain regimes optical losses can be beneficially exploited to enhance the anisotropy,^{20,21} in general, they tend to severely curtail the attainable resolution. In this view, loss compensation by means of active (gain) materials embedded in the constituent inclusions or layers has been proposed as a solution.^{22–24}

In this study, we introduce and explore a new class of extreme-parameter metamaterials that mix gain and loss in an unconventional way, based on the *parity-time* (PT) symmetry concept.²⁵ This type of symmetry, originally put forward within the framework of non-Hermitian extensions of quantum mechanics,²⁶ has pervasively permeated many branches of wave physics,²⁷ from optics and photonics^{28–30} to acoustics³¹ and elasticity.³² In essence, non-Hermitian optics leverages on

the interplay between spatially modulated losses and gain in far more sophisticated ways than a mere compensation. This brings about new, largely unexplored dimensionalities and possibilities in the synthesis of metamaterials, encompassing the entire complex plane of the constitutive parameters.

Specifically, our study focuses on a class of non-Hermitian multilayered metamaterials with alternating loss- and gain-type constituents, tailored so as to exhibit real-valued effective parameters. In particular, we show that the specific case of PT symmetry, in the ENZ limit, leads to extreme anisotropy, to which remarkable subdiffractive imaging and waveguiding/radiation responses are associated. Previous studies on PT-symmetric multilayers have unveiled several salient characteristics of their optical response, including anisotropic reflection, enhanced transmission, (anti)lasing, nonlocality, and temporal dynamics,^{33–38} but have not explored this particular regime of operation. Especially interesting appears the possibility to rely on dielectric constituents and to reconfigure the extreme anisotropy by (de)activating the gain via optical pumping. We also study nonlocal effects that can become relevant in the parameter regime of interest. Finally, we address the possible

Received: June 8, 2020

Published: August 6, 2020



implementation in terms of realistic gain materials and explore the “indefinite-parameter” regime³⁹ that results from the dispersion-induced departures from PT symmetry.

Our outcomes, which extend and generalize previous results on ENZ PT-symmetric bilayers,^{40,41} open up new vistas in the field of dielectric-based non-Hermitian metamaterials, with potentially interesting applications to reconfigurable nanophotonics and high-resolution imaging.

RESULTS AND DISCUSSION

Problem Geometry and Statement. As schematically illustrated in Figure 1a, we consider a multilayered

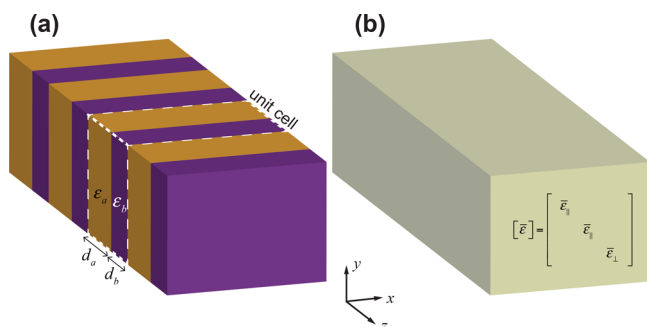


Figure 1. Problem geometry. (a) A multilayered metamaterial made of alternating loss-gain layers of thickness d_a and d_b and relative permittivity ϵ_a and ϵ_b , periodically stacked along the z -direction. The layers are assumed of infinite extent in the x - y plane. The white dashed lines delimit a unit cell. (b) Homogenized model, in terms of a uniaxially anisotropic effective medium.

metamaterial featuring two alternating constituent layers, labeled with the letters a and b , of infinite extent in the x - y plane, and stacked periodically along the z -direction. The layers have thickness d_a and d_b and are assumed as nonmagnetic; under suppressed $\exp(-i\omega t)$ time-harmonic excitation, they are characterized by complex-valued relative permittivities

$$\epsilon_a = \epsilon'_a + i\epsilon''_a, \quad \epsilon_b = \epsilon'_b - i\epsilon''_b \quad (1)$$

with the prime and double prime denoting the real and imaginary parts, respectively. Without loss of generality, we assume $\epsilon''_{a,b} > 0$, which, for the assumed time convention, implies that the “ a ”-type and “ b ”-type layers exhibit loss and gain, respectively. Moreover, to exclude from our study the well-known loss-compensated metallo-dielectric scenarios,^{22–24} we focus our attention on $\epsilon''_{a,b} > 0$.

In the limit of deeply subwavelength layers $d_{a,b} \ll \lambda$ (with $\lambda = 2\pi c/\omega$ denoting the vacuum wavelength and c the corresponding wave speed), the multilayered metamaterial can be homogenized in terms of a uniaxially anisotropic effective medium (see Figure 1b). By applying the conventional effective-medium theory (EMT), the relative-permittivity components can be expressed as Maxwell–Garnett mixing formulas⁴²

$$\bar{\epsilon}_{||} = f_a \epsilon_a + f_b \epsilon_b, \quad \bar{\epsilon}_{\perp} = \frac{\epsilon_a \epsilon_b}{f_b \epsilon_a + f_a \epsilon_b} \quad (2)$$

where $f_a = d_a/d$ and $f_b = d_b/d = 1 - f_a$ are the filling fractions and $d = d_a + d_b$ is the thickness of the unit cell (see Figure 1a).

The effective parameters in eq 2 are generally complex-valued and do not account for nonlocal (spatial dispersion)

effects. However, for certain specific combinations of the constituents, they can become real-valued, thereby indicating that, at least within the EMT approximation, loss and gain perfectly compensate. In what follows, we derive these conditions and explore certain parameter regimes for which the resulting values become *extreme*. Moreover, we also derive possible corrections to capture nonlocal effects that may become relevant.

Extreme-Parameter Regime. As detailed in the Supporting Information, by zeroing imaginary parts of the EMT parameters in eq 2, we obtain the conditions

$$\epsilon'_a = \pm \sqrt{(\epsilon'_b)^2 + (1 - \gamma^2)(\epsilon''_b)^2}, \quad f_a = \frac{1}{\gamma + 1} \quad (3)$$

where

$$\gamma = \frac{\epsilon''_a}{\epsilon''_b} > 0 \quad (4)$$

parametrizes the gain/loss (im)balance. In eq 3, the condition on the filling fraction is always physically feasible (since $\gamma > 0$), whereas, in order to ensure that ϵ'_a is consistently real-valued, we need to enforce

$$\gamma \leq \frac{|\epsilon'_b|}{\epsilon''_b} \quad (5)$$

By substituting eqs 3 and 4 in eq 2, we can finally express the real-valued effective parameters as

$$\begin{aligned} \bar{\epsilon}_{||} &= \frac{\gamma \epsilon'_b \pm \sqrt{(\epsilon'_b)^2 + (1 - \gamma^2)(\epsilon''_b)^2}}{\gamma + 1}, \\ \bar{\epsilon}_{\perp} &= \frac{\gamma \epsilon'_b \mp \sqrt{(\epsilon'_b)^2 + (1 - \gamma^2)(\epsilon''_b)^2}}{\gamma - 1} \end{aligned} \quad (6)$$

We notice that the solutions in eq 6 have two branches, corresponding to the two possible sign determinations for ϵ'_a in eq 3. Specifically, the branch corresponding to $\epsilon'_a < 0$ leads to the well-known case of loss-compensated metallo-dielectric multilayers. In particular, the extreme case $\gamma = 1$, i.e., $\epsilon''_a = \epsilon''_b$, corresponds to the so-called *resonant-gain singularity*,^{23,24} which yields $\epsilon'_a = -\epsilon'_b$, $d_a = d_b = d/2$, and hence

$$\bar{\epsilon}_{||} = 0, \quad \bar{\epsilon}_{\perp} = \infty \quad (7)$$

However, this scenario has already been extensively investigated^{22–24} and is not of interest in this study. Much more interesting is instead the branch corresponding to $\epsilon'_a > 0$. This operating regime avoids the need for a metallic component and opens to unprecedented design flexibility and subdiffractive imaging responses. Since the resolution of multilayered metamaterials is mainly determined by their periodicity, noticeable advantages stem from the possibility of using only dielectric materials whose deposition techniques allow atomically thin layers to be obtained. Moreover, the broad transparency of typical dielectrics simplifies the optical pumping of the gain component that could be freely carried out at the most convenient wavelength. Finally, the absence of a metallic component reduces the nonradiative recombination channels typical of metals. Under these assumptions, the effective parameters in eq 6 always assume *finite* values, but the ranges of variation can be broadly tailored by acting on the free parameters ϵ'_b , ϵ''_b , and γ . Of special interest is the case $\gamma = 1$, which yields $d_a = d_b = d/2$, $\epsilon'_a = \epsilon'_b = \epsilon'$, and $\epsilon''_a = \epsilon''_b = \epsilon''$. This

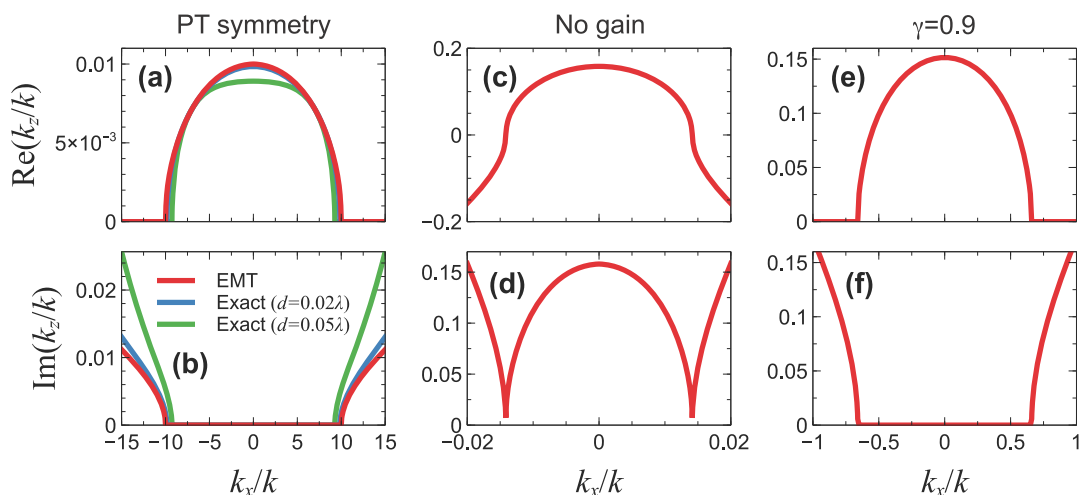


Figure 2. Dispersion characteristics. (a, b) Real and imaginary parts, respectively, of iso-frequency contours (IFCs) pertaining to a PT-symmetric parameter configuration ($\gamma = 1$) with $\epsilon' = 10^{-4}$ and $\epsilon'' = 0.1$, i.e., $\epsilon_a = 10^{-4} + i0.1$, $\epsilon_b = 10^{-4} - i0.1$, and $f_a = f_b = 0.5$. Red curves pertain to the EMT predictions from eq 10, whereas blue and green curves pertain to the exact results (see the Supporting Information for details) for $d = 0.02\lambda$ and $d = 0.05\lambda$, respectively. In view of the inherent symmetry, only the $\text{Im}(k_z) \geq 0$ branches are shown. (c, d) As in panels a and b, respectively, but in the absence of gain, i.e., $\epsilon_a = 10^{-4} + i0.1$ and $\epsilon_b = 10^{-4}$. (e, f) As in panels a and b, respectively, but for $\gamma = 0.9$, i.e., $\epsilon_a = 4.359 \times 10^{-2} + i0.09$, $\epsilon_b = 10^{-4} - i0.1$, $f_a = 0.526$, and $f_b = 0.474$. Note that in panels c–f the EMT and exact results are essentially indistinguishable.

in turn implies $\epsilon_a = \epsilon_b^*$, which, with a suitable choice of the z -axis origin, corresponds to the PT-symmetry condition²⁸

$$\epsilon(z) = \epsilon^*(-z) \quad (8)$$

It can be shown (see the Supporting Information for details) that, under these conditions, the effective parameters in eq 6 become

$$\bar{\epsilon}_{\parallel} = \epsilon', \quad \bar{\epsilon}_{\perp} = \epsilon' + \frac{(\epsilon'')^2}{\epsilon'} \quad (9)$$

While still finite, these parameters can exhibit extreme values in the ENZ limit $\epsilon' \ll 1$. Figure S1 of the Supporting Information shows, for representative values of ϵ' , the dependence of $\bar{\epsilon}_{\perp}$ on the gain/loss parameter ϵ'' ; as can be observed, quite large values (~ 100) can be attained with realistically small (< 0.1) values of the gain/loss parameter. We highlight that, in the configuration above, there is no contrast between the permittivity real parts, and therefore, these effects are solely attributable to the gain/loss interplay. These results also indicate that a broad tunability can in principle be attained by varying the concentration of the dopants and/or the optical pumping.

Canalization and Subdiffractive Imaging. To understand the basic characteristics of wave propagation in the non-Hermitian metamaterials of interest, it is insightful to start considering an infinite medium in the EMT approximation. Assuming a transverse-magnetic (TM) polarization, with y -directed magnetic field, the relevant wavevector components k_x and k_z must obey the dispersion relationship

$$\frac{k_x^2}{\bar{\epsilon}_{\perp}} + \frac{k_z^2}{\bar{\epsilon}_{\parallel}} = k^2 \quad (10)$$

where $k = \omega/c = 2\pi/\lambda$ is the wavenumber in a vacuum. In the extreme-parameter regime of interest ($\bar{\epsilon}_{\parallel} \ll 1$, $\bar{\epsilon}_{\perp} \gg 1$), eq 10 describes an ellipse with marked elongation along the k_x axis in the wavevector plane. Parts a and b of Figure 2 show (red curves) the dispersion relationship in terms of iso-frequency contours (IFCs) in the complex wavenumber plane for a PT-

symmetric configuration ($\gamma = 1$) featuring $\epsilon' = 10^{-4}$ and $\epsilon'' = 0.1$, i.e., $\epsilon_a = 10^{-4} + i0.1$, $\epsilon_b = 10^{-4} - i0.1$, and $f_a = f_b = 0.5$. As can be observed, waves with high transverse wavenumbers, up to $k_x^{(\max)} = \sqrt{\bar{\epsilon}_{\perp}} k \approx \epsilon'' k / \sqrt{\epsilon'} = 10k$, can propagate without attenuation, whereas they become evanescent (see Figure 2b) for $|k_x| > k_x^{(\max)}$. Within the propagating spectrum, the corresponding propagation constant along the z -direction is very small and weakly dependent on k_x (note the very different scales on the horizontal and vertical axes). This implies that the group velocity (orthogonal to the IFC) is predominantly z -directed, which indicates a tendency to strongly canalize the energy flow that is typical of media with extreme anisotropy.^{14–19} However, although the effects may seem similar, the underlying mechanism here is completely different from what is observed in metallo-dielectric multilayers,^{14–19} as it does not rely on the contrast between (oppositely signed) real parts of the permittivity but rather on the gain/loss interplay in the ENZ limit.

Also shown in Figure 2a and b (blue and green curves) are the exact dispersion characteristics (see the Supporting Information for details) for two representative values of the unit-cell electrical thickness. For sufficiently thin layers ($d = 0.02\lambda$), the agreement with the EMT prediction is quite good, but it starts deteriorating as the thickness increases ($d = 0.05\lambda$); this is an indication that nonlocal effects come into play. As shown in the Supporting Information (see Figure S2), more sophisticated effective-medium models^{38,43,44} can be utilized, which approximately account for these effects.

For a clearer understanding of the role of the gain/loss interplay in the extreme-parameter response, parts c and d of Figure 2 show the results pertaining to the previous configuration but in the absence of optical gain, i.e., assuming $\epsilon_a = \epsilon' + i\epsilon''$ and $\epsilon_b = \epsilon'$. In this case, the EMT parameters become $\bar{\epsilon}_{\parallel} \approx i\epsilon''/2$ and $\bar{\epsilon}_{\perp} \approx 2\epsilon'$, which yield a nearly isotropic, lossy ENZ medium. As can be expected, the IFCs are now completely different, and even waves with very low transverse wavenumbers experience a significant damping. We note that, for the parameter range of interest in this case, nonlocal effects are negligible, and the exact solutions are

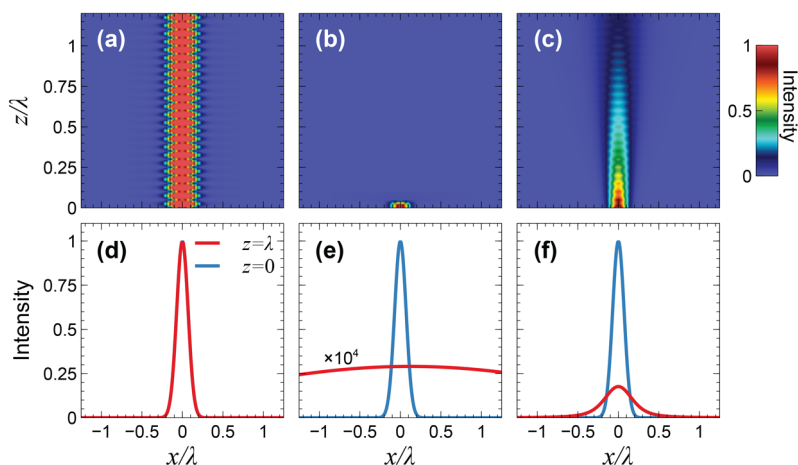


Figure 3. Canalization effects. (a–c) Numerically computed magnetic field intensity ($|H_y|^2$) maps in false-color scale pertaining to the PT-symmetric, no-gain, and $\gamma = 0.9$, respectively, parameter configurations as in Figure 2, for a multilayered metamaterial with $d = 0.05\lambda$, assuming a unit-amplitude Gaussian beam with waist $w_0 = 0.14\lambda$ launched at the plane $z = 0$. (d–f) Corresponding transverse cuts at reference planes $z = 0$ (blue curves) and $z = \lambda$ (red curves). For better visibility, the $z = \lambda$ cut in panel e is magnified by a factor of 10^4 .

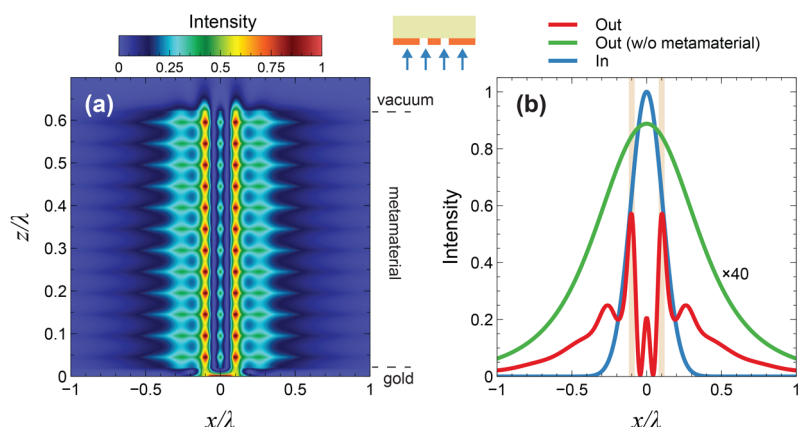


Figure 4. Subdiffractive imaging. (a) Numerically computed magnetic field intensity ($|H_y|^2$) maps in false-color scale pertaining to the PT-symmetric parameter configuration in Figures 2 and 3, for a multilayered metamaterial with $d = 0.05\lambda$ and 24 layers (total thickness of 0.6λ). The structure is excited by a unit-amplitude Gaussian beam with a waist of 0.21λ , impinging from a vacuum on a gold mask of thickness 0.02λ (laid on the metamaterial slab at $z = 0$), with two apertures of width 0.04λ centered at $x = \pm 0.1\lambda$ (see the schematic in the inset). (b) Transverse cuts of impinging beam (blue curve) and output image at the opposite end of the metamaterial slab ($z = 0.62\lambda$; red curve). Also shown (green curve), as a reference, is the output image at $z = 0.62\lambda$ in the absence of the metamaterial slab (i.e., gold mask alone), magnified by a factor of 40 for the sake of clarity. The shaded rectangles indicate the positions of the apertures.

practically indistinguishable from the EMT predictions. Figure S3 of the Supporting Information illustrates other representative cases where the PT-symmetry condition is not perfectly satisfied. It can be observed that the response is quite robust with respect to the imperfect balance of the permittivity real parts, whereas the gain/loss balance is more critical.

The last example highlights the crucial role played by the optical gain in establishing the extreme-parameter regime. However, it is important to stress that the underlying mechanism is more sophisticated than a mere loss compensation. To understand this aspect, parts e and f of Figure 2 show the results pertaining to a configuration that fulfils the real-effective-parameter conditions in eq 6 but does not satisfy the PT-symmetry condition. Specifically, while maintaining $\epsilon_b = 10^{-4} - i0.1$, we now select $\gamma = 0.9$, which yields $\epsilon_a = 4.359 \times 10^{-2} + i0.09$, $f_a = 0.526$, and $f_b = 0.474$ and in turn $\bar{\epsilon}_{\parallel} = 0.023$ and $\bar{\epsilon}_{\perp} = 0.435$. Although also for this configuration gain and loss are perfectly balanced in the mixture, as indicated by the real-valued effective parameters,

the anisotropy is much less extreme than the PT-symmetric case, resulting in a maximum transverse wavenumber $k_x^{(\max)} \approx 0.659k$, i.e., about 15 times smaller. Similar to the previous example, also in this case the nonlocal effects are essentially negligible within the parameter range of interest.

To better illustrate the implications of the above results, Figure 3 shows the propagation of a Gaussian beam with deeply subwavelength waist along a section of a multilayered metamaterial for the three parameter configurations considered. Results are computed numerically, via finite-element simulations, and pertain to an actual multilayered structure with unit-cell thickness $d = 0.05\lambda$. Specifically, parts a, b, and c of Figure 3 show the field intensity maps pertaining to the PT-symmetric, no-gain, and $\gamma = 0.9$ parameter configurations, respectively, whereas parts d, e, and f of Figure 3 show the corresponding transverse cuts at two reference planes ($z = 0$ and $z = \lambda$). As anticipated from the analysis of the IFCs, in the PT-symmetric case (Figure 3a and d), we observe a strong canalization effect: the beam propagates without transverse

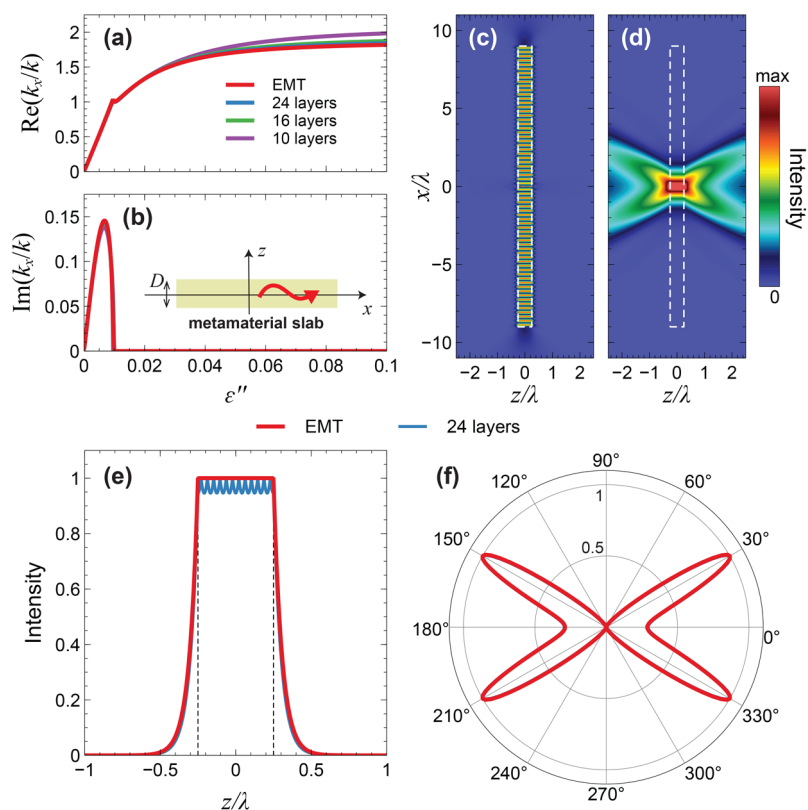


Figure 5. Waveguiding and radiation. (a, b) Real and imaginary part, respectively, of the propagation constant k_x as a function of the gain/loss parameter ϵ'' , for a PT-symmetric metamaterial slab of total thickness $D = 0.5\lambda$ (see inset), with $\epsilon' = 10^{-4}$. The red curves pertain to the EMT case; the blue, green, and purple ones pertain to multilayered structures with 24, 16, and 10 layers, respectively, corresponding to unit-cell thicknesses $d = 0.042\lambda$, 0.063λ , and 0.1λ , respectively. (c, d) Numerically computed magnetic field intensity ($|H_y|^2$) maps in false-color scale for $\epsilon'' = 0.1$ and $\epsilon'' = 5 \times 10^{-3}$, respectively. The slab is truncated along the x -direction, with a total length of 18λ (white-dashed rectangles), and is excited by a magnetic line source located at $x = y = 0$; the color scale is saturated to avoid overshadowing by the singularity. (e) Normalized transverse cuts at $z = 4\lambda$ from panel c for the EMT case (red curve) and a multilayered configuration with 24 layers (blue curve); the black-dashed lines indicate the positions of the slab interfaces. (f) Far-field (intensity) radiation patterns, computed analytically for the EMT case (red curve) and numerically from panel d (blue curve); the two curves are essentially indistinguishable. The angle is measured from the x -axis.

spread, maintaining its original shape and amplitude, in spite of the deeply subwavelength waist. However, in the absence of gain (Figure 3b and e), this effect is completely lost, and the beam experiences substantial spread and attenuation over a subwavelength propagation distance. This markedly different response suggests potentially intriguing applications to reconfigurable nanophotonics scenarios, where “on-demand” canalization effects could be induced/removed by (de)-activating the gain via optical pumping. Finally, the significant spreading observed for the parameter configuration with $\gamma = 0.9$ (Figure 3c and f) confirms the pivotal role of PT symmetry in attaining the canalization effects.

The canalization effect observed for the PT symmetry holds interesting potentials for applications to subdiffractive imaging. To give an idea, we consider a thin gold mask featuring two deeply subwavelength apertures of width 0.04λ with a center-to-center distance of 0.2λ , laid on a metamaterial slab made of 24 layers, with unit-cell period $d = 0.05\lambda$ and total thickness of 0.6λ (see the schematic in Figure 4, inset). Figure 4a shows the field map in the presence of a Gaussian-beam illumination impinging from a vacuum. We observe that the fraction of the field transmitted through the apertures is effectively canalized and the images of the apertures are well resolved at the other end of the slab, in spite of their deeply subwavelength size and separation. For a more quantitative illustration, Figure 4b

shows the transverse cuts at the input and output interfaces and also compares them with the output results in the absence of the metamaterial slab (i.e., gold mask alone). The reduced intensity of the transmitted peaks is attributable to the reflections from the gold mask.

Waveguiding and Radiation. The possibility to synthesize real-valued, extreme parameters can also be exploited to engineer unconventional in-plane waveguiding/radiation effects. Previous studies on non-Hermitian bilayers^{40,41} and trilayers⁴⁵ have demonstrated the possibility for these structures to sustain the unattenuated propagation of bound modes along the gain–loss interface(s), in ways that resemble the propagation of surface plasmon polaritons at metal–dielectric interfaces. In what follows, we extend these results to a generic multilayered configuration. To this aim, as schematically illustrated in the inset of Figure 5b, we consider a metamaterial slab of finite thickness D along the z -direction and study the propagation of *bound* modes along the x -direction, similar to conventional dielectric waveguides. These modes exhibit real-valued propagation constants k_x and exponential decay along z in the exterior region (assumed as a vacuum). In the EMT homogenized regime, the dispersion equation for the lowest-order (odd) TM modes can be written as⁴⁶

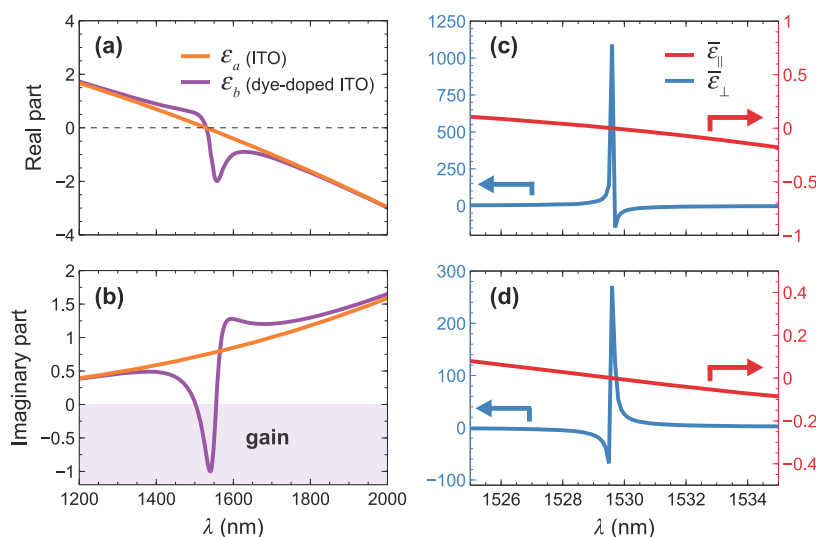


Figure 6. Possible implementation. (a, b) Real and imaginary parts, respectively, of relative permittivity for ITO (orange curves) and dye-doped ITO (purple curves) as a function of the wavelength. (c, d) Corresponding EMT parameters within a neighborhood of the ENZ wavelength; the left and right axes pertain to the orthogonal (blue curves) and parallel (red curves) components, respectively. The dashed line in panel a indicates the zero crossing.

$$k_{z0}\bar{\epsilon}_{\parallel} - ik_z \tan\left(\frac{k_z D}{2}\right) = 0 \quad (11)$$

where k_x and k_z must also obey the dispersion relationship in eq 10 and $k_{z0} = \sqrt{k^2 - k_x^2}$, $\text{Im}(k_{z0}) \geq 0$, is the z -domain wavenumber in a vacuum.

With reference to a PT-symmetric case with $\epsilon' = 10^{-4}$, parts a and b of Figure 5 show the real and imaginary parts, respectively, of the propagation constant as a function of the gain/loss parameter ϵ'' . We observe that, for values of ϵ'' beyond a threshold, the propagation constant k_x is real-valued and larger than the vacuum wavenumber k , which is indicative of a bound mode. Conversely, below such a threshold, the solutions become complex-valued, with $\text{Re}(k_x) < k$, $\text{Im}(k_x) > 0$, and $\text{Im}(k_{z0}) \leq 0$. These solutions represent leaky modes which can couple with the radiation continuum; although seemingly unphysical (as they decay along the x -direction and grow exponentially along the z -direction), they can be effectively utilized to model radiation characteristics.⁴⁷ As one may intuitively expect, the bound and leaky regions correspond to the guiding ($\bar{\epsilon}_{\perp} > 1$) and antiguiding ($\bar{\epsilon}_{\perp} < 1$) regimes, respectively, with the threshold condition $\epsilon'' \approx 0.01$ yielding $\bar{\epsilon}_{\perp} = 1$ (see Figure S1 of the Supporting Information). Also shown in Figure 5a and b are the solutions pertaining to actual multilayers, with various numbers of layers. As can be observed, the results agree fairly well with the EMT predictions within the leaky-mode region.

Within the bound-mode region, some differences are visible, which become more evident for smaller numbers of layers (i.e., electrically thicker unit cells) as a consequence of the increasingly relevant nonlocal effects. Parts c and d of Figure 5 show the numerically computed field distributions pertaining to two representative guided and leaky modes, respectively. Specifically, from Figure 5c, we observe that the field is well confined within the slab, with the visible standing-wave pattern attributable to the structure truncation along the x -direction. For the same configuration, Figure 5e compares a transverse cut with the theoretical EMT prediction, showing a good agreement. The only visible difference in the magnetic-field

distribution is that the EMT prediction is essentially constant within the slab (consistent with the ENZ condition $\bar{\epsilon}_{\parallel} \ll 1$), whereas for the multilayer case it is mildly peaked at the gain/loss interfaces. From Figure 5d, the leakage effects and the field decay along the x -direction are evident. The corresponding far-field radiation pattern, shown in Figure 5f, is typical of leaky-wave antennas,⁴⁷ and in excellent agreement with the theoretical prediction based on the complex-valued propagation constant pertaining to the EMT case (see the Supporting Information for details). By simple reciprocity arguments, as was already observed for PT-symmetric bilayers,⁴⁰ in this regime, an obliquely incident plane wave can tunnel through the slab without any reflection.

For fixed values of the gain/loss parameter ϵ'' , the propagation constant can be further tuned by changing the slab electrical thickness D/λ . This is quantitatively illustrated in Figure S4 of the Supporting Information for both the bound and leaky regimes. As can be observed, for electrically thicker slabs, nonlocal effects become more visible in the bound-mode regime, yielding significant departures from the EMT prediction and strong dispersion effects.

It is quite remarkable that, although in the ENZ limit both material constituents operate in the antiguiding regime $\epsilon' < 1$, the interplay between gain and loss arising from their combination enables wave confinement and unattenuated guiding. Also in this scenario, the role played by PT symmetry and gain–loss balance is pivotal. To give an idea, for the same variation range of ϵ'' , a configuration with $\gamma = 0.9$ would result in $\bar{\epsilon}_{\perp} \leq 0.453$, thereby always operating in the antiguiding regime. Moreover, as previously discussed, turning off the gain in the PT-symmetric configuration would basically remove the extreme anisotropy, yielding a quasi-isotropic lossy ENZ medium. In this regime, it is well-known that an electrically thin slab excited by a line source would essentially radiate a very directive beam along the direction orthogonal to the interface.⁴⁸ Once again, one may envision applications to reconfigurable scenarios where “on-demand” waveguiding/radiation effects can be (de)activated or radically changed via optical pumping.

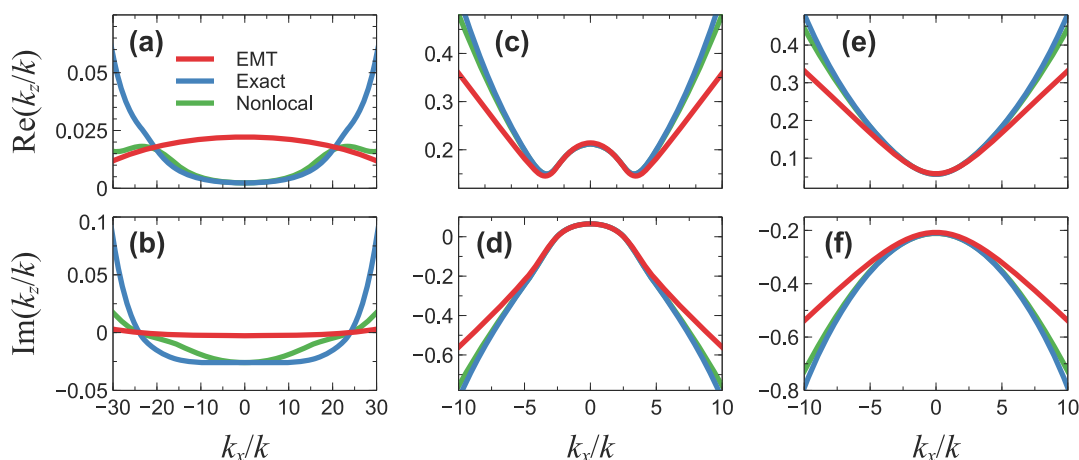


Figure 7. Dispersion characteristics. (a, b) Real and imaginary parts, respectively, of iso-frequency contours (IFCs) pertaining to a configuration with realistic materials as in Figure 6, at $\lambda = 1529.6$ nm ($\epsilon_a = 5.135 \times 10^{-4} + i0.747$, $\epsilon_b = 4.508 \times 10^{-4} - i0.747$), with $f_a = f_b = 0.5$ and $d = 0.05\lambda$. Red curves pertain to the EMT predictions from eq 10, whereas blue and green curves pertain to the exact and nonlocal-effective models, respectively (see the Supporting Information for details). In view of the inherent symmetry, only the $\text{Re}(k_z) \geq 0$ branches are shown. (c, d) As in panels a and b, respectively, but at $\lambda = 1528$ nm ($\epsilon_a = 9.440 \times 10^{-3} + i0.745$, $\epsilon_b = 7.391 \times 10^{-2} - i0.689$). (e, f) As in panels a and b, respectively, but at $\lambda = 1531$ nm ($\epsilon_a = -7.310 \times 10^{-3} + i0.749$, $\epsilon_b = -7.232 \times 10^{-2} - i0.798$).

Finally, we note in passing that, like all non-Hermitian systems, our multilayered metamaterials can in principle exhibit *exceptional points*, i.e., spectral degeneracies implying the coalescence of two or more eigenstates into one, with the same complex-valued eigenvalue.³⁰ For PT-symmetric structures, a typical manifestation is the so-called “spontaneous symmetry breaking”,²⁵ i.e., an abrupt transition from a real- to a complex-valued eigenspectrum beyond a critical threshold of the loss/gain level (or, equivalently, the layer electrical thickness). However, we verified that this threshold is far beyond the parameter regime of interest here, featuring deeply subwavelength layers and realistically small levels of the gain/loss parameter.

Possible Implementation. Although the main focus of our study is on the basic phenomenological aspects, in anticipation of future experimental validations, it is important to assess the actual feasibility of the extreme-parameter conditions of interest. From the physical viewpoint, it is well-known that causality dictates that the PT-symmetry condition cannot be exactly satisfied over extended spectral ranges but only at isolated wavelengths.⁴⁹ For the lossy ENZ material, indium tin oxide (ITO) is an excellent candidate, as it naturally exhibits an ENZ response at infrared wavelengths. Parts a and b of Figure 6 show (orange curves) its relative permittivity at near-infrared wavelengths, computed via a well-known Drude–Lorentz model;⁵⁰ as can be observed, at a wavelength of ~ 1530 nm, the real part of the permittivity vanishes.

The gain material can be synthesized by doping a dielectric host medium with dyes. For our purposes, it is very convenient to select ITO itself as the dielectric host, since this naturally ensures $\epsilon'_a \approx \epsilon'_b$. Moreover, the broad availability of ITO photoluminescent nanoparticles, inks, and powders further justifies our choice.^{51–53} In what follows, we utilize a well-established approximate (linearized) model for the relative permittivity, with the gain medium modeled as a four-level system:⁵⁴

$$\epsilon_b(\omega) = \epsilon_h + \frac{\sigma_a}{(\omega^2 + i\Delta\omega_a\omega - \omega_a^2)} \times \frac{(\tau_{21} - \tau_{10})\Gamma_{\text{pump}}}{[1 + (\tau_{32} + \tau_{21} + \tau_{10})\Gamma_{\text{pump}}]}\bar{N}_0 \quad (12)$$

In eq 12, ϵ_h is the relative permittivity of the host medium, and all other parameters are defined in Table S1 of the Supporting Information.

To match the ENZ wavelength of ITO at ~ 1530 nm, optical transitions occurring in lanthanides are especially suited.⁵⁵ This is the case, for instance, of a particular organic/inorganic $\text{NaYF}_4:\text{Yb}^{3+}/\text{X}^{3+}@\text{NaYbF}_4@\text{NaYF}_4:\text{Nd}^{3+}$ ($\text{X} = \text{Er}$) core/shell/shell (CSS) nanocrystal architecture, functionalized with indocyanine green (ICG) dye on the surface.⁵⁶ The emission bands of this structure can be optimized within the so-called *second biological window of transparency* (NIR-II, 1000–1700 nm), and hence, its emission can be engineered to match the ENZ wavelength of ITO.^{56,57} Moreover, these structures allow for a broad excitable spectral range (700–860 nm). For our example, we select the 1550 nm transition related to the ICG sensitized Er^{3+} doped CSS nanocrystals, assuming an excitation at 800 nm with a pulsed laser. The corresponding values of all relevant parameters in eq 12 are given in Table S1 of the Supporting Information. The resulting relative permittivity of the dye-doped ITO is also shown (purple curves) in Figure 6a and b, from which we observe the ENZ response around 1530 nm, accompanied by a negative peak of the imaginary part (i.e., gain).

Accordingly, at the wavelength $\lambda = 1529.6$ nm, the PT-symmetry condition is almost exactly satisfied, with $\epsilon_a = 5.135 \times 10^{-4} + i0.747$ and $\epsilon_b = 4.508 \times 10^{-4} - i0.747$. Parts c and d of Figure 6 show the resulting EMT parameters, within a reduced spectral range centered around the ENZ wavelength. We observe the expected zero-crossing of the parallel component and a very sharp variation of the orthogonal one, with a dynamic range of thousands in magnitude and a spectral line shape that resembles what is observed for resonant-gain singularities in metallo-dielectric metamaterials.²³ Specifically, at the ENZ wavelength $\lambda = 1529.6$ nm, we obtain $\bar{\epsilon}_{\parallel} = 4.82 \times$

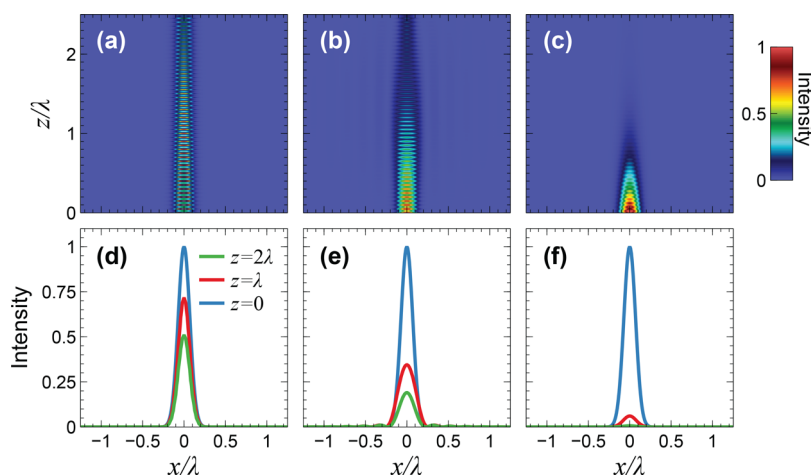


Figure 8. Canalization effects. (a–c) Numerically computed magnetic field intensity ($|H_y|^2$) maps in false-color scale pertaining to the (quasi)PT-symmetric and indefinite-parameter configurations ($\lambda = 1529.6, 1528$, and 1531 nm, respectively) as in Figure 7, for a multilayered metamaterial with $d = 0.05\lambda$, assuming a unit-amplitude Gaussian beam with waist $w_0 = 0.14\lambda$ launched at the plane $z = 0$. (d–f) Corresponding transverse cuts at reference planes $z = 0$ (blue curves), $z = \lambda$ (red curves), and $z = 2\lambda$ (green curves).

$10^{-4} - i1.2 \times 10^{-4}$ and $\bar{\epsilon}_\perp = 1091.02 + i271.5$, with the residual imaginary parts attributable to the slightly imperfect PT-symmetry condition. At smaller wavelengths, the real parts of the effective parameters are both positive and the imaginary parts have opposite signs; at larger wavelengths, both real parts become negative, with the imaginary parts maintaining opposite signs. These types of “indefinite” non-Hermitian metamaterials exhibit loss and gain along different axes and do not display a clear-cut passive/active character; depending on the propagation direction, either attenuation or amplification may prevail.³⁹ Interestingly, these media also arise within the framework of non-Hermitian (complex-coordinate) transformation optics.^{58,59}

Figure 7 shows the IFCs pertaining to the (quasi)PT-symmetric case and two representative indefinite configurations. For the (quasi)PT-symmetric case (Figure 7a and b), the EMT results show a broad wavenumber range with the expected flat, concave-down behavior and a very small (negative) imaginary part; at higher wavenumbers, the imaginary part becomes positive and grows to sensible values, resulting in a cutoff. This is qualitatively similar to what is observed in the idealized-parameter scenario (cf. Figure 2a and b). However, there are some visible differences between the exact results and the EMT predictions, whereas the agreement improves sensibly when nonlocal corrections are taken into account (see the Supporting Information for details). In particular, the imaginary part of k_z exhibits moderately small negative values for most of the range of interest.

Parts c and d of Figure 7 pertain instead to slightly smaller wavelength, yielding indefinite effective parameters with positive real parts ($\bar{\epsilon}_\parallel = 0.042 + i0.029$ and $\bar{\epsilon}_\perp = 9.07 - i4.90$). We now observe that the imaginary part of k_z remains small and positive within a sizable spectral region and then becomes negative and growing in magnitude. For this parameter configuration, the agreement between EMT and exact results looks better and is further improved by the nonlocal corrections.

Finally, parts e and f of Figure 7 illustrate the response at a slightly larger wavelength, corresponding to indefinite effective parameters with negative real parts ($\bar{\epsilon}_\parallel = -0.04 - i0.02$ and $\bar{\epsilon}_\perp = -10.44 + i7.55$). In this case, the imaginary part of k_z is always negative.

For the assumed time-harmonic dependence, the conventional choice $\text{Re}(k_z) > 0$ of the branch-cut for the solution would therefore imply exponential amplification for most of the spectral wavenumbers of interest. However, it is worth emphasizing that the parameter configurations above entail a complex interplay among loss, gain, and possibly evanescence effects, and an *a priori* choice of the branch-cut is neither straightforward nor necessarily meaningful, especially when unbounded domains and sources are assumed. To give an idea, for the canonical problem of total internal reflection from a gain medium, such choice remains a controversial issue, and the related concept of “evanescent gain” is still debated.^{60–63} In particular, some evidence suggests a counterintuitive sign flip in the propagation constant of the gain medium for incidence beyond the critical angle.⁶³ Likewise, for the parameter configurations in Figure 7, numerical (finite-element) evidence indicates that most of the spectral wavenumber components in fact experience an exponential decay, with attenuation ranging from mild (Figure 7b) to significant (Figure 7f), thereby suggesting $\text{Re}(k_z) < 0$ as the proper branch-cut.

For a clearer illustration, we study the propagation of a Gaussian beam with subwavelength waist, as shown in Figure 8. For the (quasi)PT-symmetric case (Figure 8a and b), we still observe the canalization effects, though accompanied by mild attenuation, attributable to the imperfect gain/loss balance. Interestingly, some moderate canalization effects are also visible for the indefinite parameter configuration with positive real parts (Figure 8c and d), although the attenuation is more pronounced. In principle, one could engineer the material dispersion in different ways, tailoring the gain/loss imbalance so as to attain an amplification effect. Finally, for the indefinite parameter configuration with negative real parts (Figure 8e and f), the inherent evanescent character combined with the gain/loss imbalance strongly curtails the canalization effect.

Overall, the above results indicate that the extreme-parameter conditions of interest can be in principle synthesized, within very narrow frequency/wavelength ranges, by relying on realistic material constituents.

CONCLUSIONS

To sum up, we have put forward and investigated a class of non-Hermitian multilayered metamaterials that can exhibit extreme anisotropy due to a peculiar interplay between gain and loss in the ENZ regime. We have illustrated several unusual propagation phenomena that can occur in these media (including subdiffractive imaging, waveguiding, and radiation), pointing out similarities and fundamental differences with metallo-dielectric multilayers and highlighting the broad tunability and reconfigurability attainable in principle by tailoring the gain constituent via optical pumping. Finally, we have addressed a technologically feasible implementation based on ITO and dye-doped ITO and have explored the effects of realistic material dispersion.

Overall, our results uncover a largely unexplored extreme-parameter regime in non-Hermitian optics, which may inspire the development of novel dielectric-based systems and components for reconfigurable nanophotonics. Current and future studies are accordingly aimed at a deeper investigation of the application-oriented aspects and a possible experimental realization. Also of great interest are possible extensions and generalizations to cylindrical and spherical geometries, as well as flat-optics scenarios based on 2-D material constituents.

METHODS

Analytic Modeling. The analytic derivation of the nonlocal corrections in the EMT model, as well as of the dispersion equations for the waveguiding/radiation in multilayered structures, is detailed in the [Supporting Information](#). The dispersion equations are implemented numerically in Python and solved via the `broyden1` nonlinear solver available in the SciPy library.⁶⁴

Numerical Simulations. For the finite-element numerical simulations, we rely on the RF module of the commercial software package COMSOL Multiphysics.⁶⁵ In particular, for the field maps in [Figures 3](#) and [8](#), an infinite structure is simulated, with the computational domain terminated by a perfectly matched layer (PML) tailored on the EMT parameters. The Gaussian-beam illumination is synthesized as a hard source. For the configuration in [Figure 4](#), a layer of vacuum is introduced at the top end of the structure. At the bottom end, there is a gold layer modeled with a relative permittivity of $\epsilon_{\text{Au}} = -8.495 + i1.624$ compatible with realistic values at infrared wavelengths.⁶⁶ Finally, the waveguiding configurations in [Figure 5](#) are embedded in a vacuum (with a suitable PML termination) and excited by a magnetic line source at the center. The far-field radiation patterns are computed by means of the `farfield` postprocessing option. For all simulations, a standard adaptive meshing with maximum element size of 0.1λ in the vacuum regions and $d/10$ in the multilayered structures, resulting in a number of degrees of freedom ranging from 5 to 15 million. For the solution of the system, the MUMPS solver is utilized with default parameters.

ASSOCIATED CONTENT

Supporting Information

The Supporting Information is available free of charge at <https://pubs.acs.org/doi/10.1021/acsp Photonics.0c00924>.

Details on analytic derivations, additional results, and details on gain material ([PDF](#))

AUTHOR INFORMATION

Corresponding Author

Vincenzo Galdi – *Fields & Waves Lab, Department of Engineering, University of Sannio, I-82100 Benevento, Italy;*
orcid.org/0000-0002-4796-3600; Email: vgaldi@unisannio.it

Authors

Marino Coppolaro – *Fields & Waves Lab, Department of Engineering, University of Sannio, I-82100 Benevento, Italy*

Massimo Moccia – *Fields & Waves Lab, Department of Engineering, University of Sannio, I-82100 Benevento, Italy*

Vincenzo Caligiuri – *Department of Physics and CNR – Nanotec, University of Calabria, I-87036 Rende, CS, Italy;*
orcid.org/0000-0003-1035-4702

Giuseppe Castaldi – *Fields & Waves Lab, Department of Engineering, University of Sannio, I-82100 Benevento, Italy*

Nader Engheta – *Department of Electrical and Systems Engineering, University of Pennsylvania, Philadelphia, Pennsylvania 19104-6314, United States*

Complete contact information is available at:
<https://pubs.acs.org/10.1021/acsp Photonics.0c00924>

Author Contributions

G.C., N.E., and V.G. conceived the idea. M.C., G.C., and V.G. developed the analytical framework. M.C. and M.M. carried out the numerical simulations. V.C. developed the realistic models for the gain and loss media. V.G. and N.E. supervised the study. All authors participated in the data analysis and interpretation. V.G. wrote the manuscript, with inputs and feedback from all authors.

Notes

The authors declare no competing financial interest.

ACKNOWLEDGMENTS

This work was supported in part by the University of Sannio (FRA program). N.E. acknowledges partial support from the Vannevar Bush Faculty Fellowship program sponsored by the Basic Research Office of the Assistant Secretary of Defense for Research and Engineering and funded by the Office of Naval Research through grant N00014-16-1-2029.

REFERENCES

- (1) Capolino, F. *Theory and Phenomena of Metamaterials*; CRC Press: 2009.
- (2) Cai, W.; Shalaev, V. M. *Optical Metamaterials: Fundamentals and Applications*; Springer: New York, 2010.
- (3) Sihvola, A.; Tretyakov, S.; de Baas, A. Metamaterials with Extreme Material Parameters. *J. Commun. Technol. Electron.* **2007**, *52*, 986–990.
- (4) Silveirinha, M.; Engheta, N. Tunneling of Electromagnetic Energy through Subwavelength Channels and Bends Using ϵ -Near-Zero Materials. *Phys. Rev. Lett.* **2006**, *97*, 157403.
- (5) Reshef, O.; Leon, I. D.; Alam, M. Z.; Boyd, R. W. Nonlinear Optical Effects in Epsilon-near-Zero Media. *Nat. Rev. Mater.* **2019**, *4*, 535–551.
- (6) Davoyan, A. R.; Mahmoud, A. M.; Engheta, N. Optical Isolation with Epsilon-near-Zero Metamaterials. *Opt. Express* **2013**, *21*, 3279–3286.
- (7) Liberal, I.; Engheta, N. The Rise of Near-Zero-Index Technologies. *Science* **2017**, *358*, 1540–1541.
- (8) Fleury, R.; Alù, A. Enhanced Superradiance in Epsilon-near-Zero Plasmonic Channels. *Phys. Rev. B: Condens. Matter Mater. Phys.* **2013**, *87*, 201101.

- (9) Niu, X.; Hu, X.; Chu, S.; Gong, Q. Epsilon-Near-Zero Photonics: A New Platform for Integrated Devices. *Adv. Opt. Mater.* **2018**, *6*, 1701292.
- (10) Liberal, I.; Engheta, N. Near-Zero Refractive Index Photonics. *Nat. Photonics* **2017**, *11*, 149–158.
- (11) Liberal, I.; Mahmoud, A. M.; Engheta, N. Geometry-Invariant Resonant Cavities. *Nat. Commun.* **2016**, *7*, 10989.
- (12) Silveirinha, M. G. Trapping Light in Open Plasmonic Nanostructures. *Phys. Rev. A: At., Mol., Opt. Phys.* **2014**, *89*, No. 023813.
- (13) Elser, J.; Wangberg, R.; Podolskiy, V. A. Nanowire Metamaterials with Extreme Optical Anisotropy. *Appl. Phys. Lett.* **2006**, *89*, 261102.
- (14) Salandrino, A.; Engheta, N. Far-Field Subdiffraction Optical Microscopy Using Metamaterial Crystals: Theory and Simulations. *Phys. Rev. B: Condens. Matter Mater. Phys.* **2006**, *74*, No. 075103.
- (15) Ramakrishna, S. A.; Pendry, J. B.; Wiltshire, M. C. K.; Stewart, W. J. Imaging the near Field. *J. Mod. Opt.* **2003**, *50*, 1419–1430.
- (16) Cai, W.; Genov, D. A.; Shalae, V. M. Superlens Based on Metal-Dielectric Composites. *Phys. Rev. B: Condens. Matter Mater. Phys.* **2005**, *72*, 193101.
- (17) Wood, B.; Pendry, J. B.; Tsai, D. P. Directed Subwavelength Imaging Using a Layered Metal-Dielectric System. *Phys. Rev. B: Condens. Matter Mater. Phys.* **2006**, *74*, 115116.
- (18) Belov, P. A.; Hao, Y. Subwavelength Imaging at Optical Frequencies Using a Transmission Device Formed by a Periodic Layered Metal-Dielectric Structure Operating in the Canalization Regime. *Phys. Rev. B: Condens. Matter Mater. Phys.* **2006**, *73*, 113110.
- (19) Belov, P. A.; Zhao, Y.; Hao, Y.; Parini, C. Enhancement of Evanescent Spatial Harmonics inside Media with Extreme Optical Anisotropy. *Opt. Lett.* **2009**, *34*, 527–529.
- (20) Feng, S. Loss-Induced Omnidirectional Bending to the Normal in ϵ -Near-Zero Metamaterials. *Phys. Rev. Lett.* **2012**, *108*, 193904.
- (21) Shen, N.-H.; Zhang, P.; Koschny, T.; Soukoulis, C. Metamaterial-Based Lossy Anisotropic Epsilon-near-Zero Medium for Energy Collimation. *Phys. Rev. B: Condens. Matter Mater. Phys.* **2016**, *93*, 245118.
- (22) Ramakrishna, S. A.; Pendry, J. B. Removal of Absorption and Increase in Resolution in a Near-Field Lens via Optical Gain. *Phys. Rev. B: Condens. Matter Mater. Phys.* **2003**, *67*, 201101.
- (23) Caligiuri, V.; Pezzi, L.; Veltri, A.; De Luca, A. Resonant Gain Singularities in 1D and 3D Metal/Dielectric Multilayered Nanostructures. *ACS Nano* **2017**, *11*, 1012–1025.
- (24) Caligiuri, V.; Dhama, R.; Sreekanth, K. V.; Strangi, G.; De Luca, A. Dielectric Singularity in Hyperbolic Metamaterials: The Inversion Point of Coexisting Anisotropies. *Sci. Rep.* **2016**, *6*, 20002.
- (25) Bender, C. M.; Boettcher, S. Real Spectra in Non-Hermitian Hamiltonians Having PT Symmetry. *Phys. Rev. Lett.* **1998**, *80*, 5243–5246.
- (26) Bender, C. M. Making Sense of Non-Hermitian Hamiltonians. *Rep. Prog. Phys.* **2007**, *70*, 947–1018.
- (27) El-Ganainy, R.; Makris, K. G.; Khajavikhan, M.; Musslimani, Z. H.; Rotter, S.; Christodoulides, D. N. Non-Hermitian Physics and PT Symmetry. *Nat. Phys.* **2018**, *14*, 11–19.
- (28) Feng, L.; El-Ganainy, R.; Ge, L. Non-Hermitian Photonics Based on Parity–Time Symmetry. *Nat. Photonics* **2017**, *11*, 752–762.
- (29) El-Ganainy, R.; Khajavikhan, M.; Christodoulides, D. N.; Özdemir, S. K. The Dawn of Non-Hermitian Optics. *Commun. Phys.* **2019**, *2*, 37.
- (30) Özdemir, S. K.; Rotter, S.; Nori, F.; Yang, L. Parity–Time Symmetry and Exceptional Points in Photonics. *Nat. Mater.* **2019**, *18*, 783–798.
- (31) Zhu, X.; Ramezani, H.; Shi, C.; Zhu, J.; Zhang, X. PT-Symmetric Acoustics. *Phys. Rev. X* **2014**, *4*, No. 031042.
- (32) Scheibner, C.; Souslov, A.; Banerjee, D.; Surówka, P.; Irvine, W. T. M.; Vitelli, V. Odd Elasticity. *Nat. Phys.* **2020**, *16*, 475–480.
- (33) Zhu, X.-F.; Peng, Y.-G.; Zhao, D.-G. Anisotropic Reflection Oscillation in Periodic Multilayer Structures of Parity-Time Symmetry. *Opt. Express* **2014**, *22*, 18401–18411.
- (34) Ding, S.; Wang, G. P. Extraordinary Reflection and Transmission with Direction Dependent Wavelength Selectivity Based on Parity-Time-Symmetric Multilayers. *J. Appl. Phys.* **2015**, *117*, No. 023104.
- (35) Novitsky, D. V.; Tuz, V. R.; Prosvirnin, S. L.; Lavrinenko, A. V.; Novitsky, A. V. Transmission Enhancement in Loss-Gain Multilayers by Resonant Suppression of Reflection. *Phys. Rev. B: Condens. Matter Mater. Phys.* **2017**, *96*, 235129.
- (36) Novitsky, D. V.; Karabchevsky, A.; Lavrinenko, A. V.; Shalin, A. S.; Novitsky, A. V. PT Symmetry Breaking in Multilayers with Resonant Loss and Gain Locks Light Propagation Direction. *Phys. Rev. B: Condens. Matter Mater. Phys.* **2018**, *98*, 125102.
- (37) Novitsky, D. V. CPA-Laser Effect and Exceptional Points in PT-Symmetric Multilayer Structures. *J. Opt.* **2019**, *21*, No. 085101.
- (38) Novitsky, D. V.; Shalin, A. S.; Novitsky, A. Nonlocal Homogenization of PT-Symmetric Multilayered Structures. *Phys. Rev. A: At., Mol., Opt. Phys.* **2019**, *99*, No. 043812.
- (39) Mackay, T. G.; Lakhtakia, A. Dynamically Controllable Anisotropic Metamaterials with Simultaneous Attenuation and Amplification. *Phys. Rev. A: At., Mol., Opt. Phys.* **2015**, *92*, No. 053847.
- (40) Savoia, S.; Castaldi, G.; Galdi, V.; Alù, A.; Engheta, N. Tunneling of Obliquely Incident Waves through PT-Symmetric Epsilon-near-Zero Bilayers. *Phys. Rev. B: Condens. Matter Mater. Phys.* **2014**, *89*, No. 085105.
- (41) Savoia, S.; Castaldi, G.; Galdi, V.; Alù, A.; Engheta, N. PT-Symmetry-Induced Wave Confinement and Guiding in ϵ -near-Zero Metamaterials. *Phys. Rev. B: Condens. Matter Mater. Phys.* **2015**, *91*, 115114.
- (42) Sihvola, A. H. *Electromagnetic Mixing Formulas and Applications*; IET: Stevenage, U.K., 1999.
- (43) Chern, R.-L. Spatial Dispersion and Nonlocal Effective Permittivity for Periodic Layered Metamaterials. *Opt. Express* **2013**, *21*, 16514–16527.
- (44) Popov, V.; Lavrinenko, A. V.; Novitsky, A. Operator Approach to Effective Medium Theory to Overcome a Breakdown of Maxwell Garnett Approximation. *Phys. Rev. B: Condens. Matter Mater. Phys.* **2016**, *94*, No. 085428.
- (45) Savoia, S.; Castaldi, G.; Galdi, V. Non-Hermiticity-Induced Wave Confinement and Guiding in Loss-Gain-Loss Three-Layer Systems. *Phys. Rev. A: At., Mol., Opt. Phys.* **2016**, *94*, No. 043838.
- (46) Lindell, I. V.; Ilvonen, S. Waves in a Slab of Uniaxial BW Medium. *J. Electromagn. Waves Appl.* **2002**, *16*, 303–318.
- (47) Jackson, D. R.; Oliner, A. A. Leaky-Wave Antennas. In *Modern Antenna Handbook*; Balanis, C. A., Ed; John Wiley & Sons: New York, 2007; pp 325–367.
- (48) Enoch, S.; Tayeb, G.; Sabouroux, P.; Guérin, N.; Vincent, P. A Metamaterial for Directive Emission. *Phys. Rev. Lett.* **2002**, *89*, 213902.
- (49) Zyablovsky, A. A.; Vinogradov, A. P.; Dorofeenko, A. V.; Pukhov, A. A.; Lisyansky, A. A. Causality and Phase Transitions in PT-Symmetric Optical Systems. *Phys. Rev. A: At., Mol., Opt. Phys.* **2014**, *89*, No. 033808.
- (50) D'Elia, S.; Scaramuzza, N.; Ciuchi, F.; Versace, C.; Strangi, G.; Bartolino, R. Ellipsometry Investigation of the Effects of Annealing Temperature on the Optical Properties of Indium Tin Oxide Thin Films Studied by Drude-Lorentz Model. *Appl. Surf. Sci.* **2009**, *255*, 7203–7211.
- (51) Jang, H. D.; Seong, C. M.; Chang, H. K.; Kim, H. C. Synthesis and Characterization of Indium–Tin Oxide (ITO) Nanoparticles. *Curr. Appl. Phys.* **2006**, *6*, 1044–1047.
- (52) Sun, Z.; He, J.; Kumbhar, A.; Fang, J. Nonaqueous Synthesis and Photoluminescence of ITO Nanoparticles. *Langmuir* **2010**, *26*, 4246–4250.
- (53) Ito, D.; Masuko, K.; Weintraub, B. A.; McKenzie, L. C.; Hutchison, J. E. Convenient Preparation of ITO Nanoparticles Inks for Transparent Conductive Thin Films. *J. Nanopart. Res.* **2012**, *14*, 1274.

- (54) Campione, S.; Albani, M.; Capolino, F. Complex Modes and Near-Zero Permittivity in 3D Arrays of Plasmonic Nanoshells: Loss Compensation Using Gain. *Opt. Mater. Express* **2011**, *1*, 1077–1089.
- (55) Binnemans, K. Lanthanide-Based Luminescent Hybrid Materials. *Chem. Rev.* **2009**, *109*, 4283–4374.
- (56) Shao, W.; Chen, G.; Kuzmin, A.; Kutscher, H. L.; Pliss, A.; Ohulchanskyy, T. Y.; Prasad, P. N. Tunable Narrow Band Emissions from Dye-Sensitized Core/Shell/Shell Nanocrystals in the Second Near-Infrared Biological Window. *J. Am. Chem. Soc.* **2016**, *138*, 16192–16195.
- (57) Lin, H.; Xu, D.; Li, Y.; Yao, L.; Xu, L.; Ma, Y.; Yang, S.; Zhang, Y. Intense Red Upconversion Luminescence in Er³⁺-Sensitized Particles through Confining the 1532 Nm Excitation Energy. *J. Lumin.* **2019**, *216*, 116731.
- (58) Savoia, S.; Castaldi, G.; Galdi, V. Complex-Coordinate Non-Hermitian Transformation Optics. *J. Opt.* **2016**, *18*, No. 044027.
- (59) Castaldi, G.; Savoia, S.; Galdi, V.; Alù, A.; Engheta, N. PT Metamaterials via Complex-Coordinate Transformation Optics. *Phys. Rev. Lett.* **2013**, *110*, 173901.
- (60) Romanov, G. N.; Shakhidzhanov, S. S. Amplification of Electromagnetic Field in Total Internal Reflection from a Region of Inverted Population. *JETP Lett.* **1972**, *16*, 209–211.
- (61) Willis, K. J.; Schneider, J. B.; Hagness, S. C. Amplified Total Internal Reflection: Theory, Analysis, and Demonstration of Existence via FDTD. *Opt. Express* **2008**, *16*, 1903–1914.
- (62) Grepstad, J. O.; Skaar, J. Total Internal Reflection and Evanescent Gain. *Opt. Express* **2011**, *19* (22), 21404–21418.
- (63) Herzig Sheinfux, H.; Zhen, B.; Kaminer, I.; Segev, M. Total Internal Reflection in Gain Media. In *CLEO: 2015*; OSA: San Jose, CA, 2015; p FM2D.3.
- (64) SciPy — SciPy v1.4.1 Reference Guide. <https://docs.scipy.org/doc/scipy/reference/> (accessed July 16, 2020).
- (65) COMSOL Multiphysics, v. 5.1; COMSOL AB: Stockholm, Sweden, 2015.
- (66) Johnson, P. B.; Christy, R. W. Optical Constants of the Noble Metals. *Phys. Rev. B* **1972**, *6*, 4370–4379.